Journal of Materials Chemistry C

ROYAL SOCIETY OF CHEMISTRY

COMMUNICATION

View Article Online
View Journal | View Issue

Cite this: J. Mater. Chem. C, 2020, 8, 11360

Received 8th June 2020,
Accepted 5th August 2020

DOI: 10.1039/d0tc02706e

rsc.li/materials-c

Low defects density $CsPbBr_3$ single crystals grown by an additive assisted method for gamma-ray detection†

Yuanxiang Feng,[a] Lei Pan,[b] Haotong Wei,[a] Ye Liu,[a] Zhenyi Ni,[a] Jingjing Zhao,[a] Peter N. Rudd,[a] Lei R. Cao[b] and Jinsong Huang*[a]

Metal halide perovskites have arisen as a new family of semiconductors for radiation detectors due to their high stopping power, large and balanced electron–hole mobility-lifetime ($\mu\tau$) product, and tunable bandgap. Here, we report a simple and low-cost solution processing approach using additive-assisted inverse temperature crystallization (ITC) to grow cesium lead bromide ($CsPbBr_3$) single crystals with low-defect density. Crystals grown from precursor solutions without additives tend to grow fastest along the [002] direction, resulting in crystals shaped as small elongated bars. The addition of choline bromide (CB) proves to mediate the crystallization process to produce large single crystals with a cuboid shape, allowing for more practical fabrication of gamma-ray detectors. This new additive-assisted growth method also improves the resulting crystal quality to yield a reduction in the density of trap states by over one order of magnitude, relative to a crystal grown without CB. The detector fabricated from a CB-assisted solution-grown perovskite $CsPbBr_3$ single crystal is able to acquire an energy spectrum from a cesium-137 (^{137}Cs) source with a resolution of 5.5% at 662 keV.

Introduction

Nuclear radiation detectors are capturing growing attention due to the broad potential application in materials science, physics research, nuclear energy, medical imaging, and radiation safety.[1–4] Gamma-ray spectroscopy, which is able to resolve the energy of the incoming gamma-ray and identify the radioactive species and isotopes, is a critical sector in the radiation detection market. Germanium (Ge) is one of the most developed semiconductors which has been successfully employed in gamma-ray spectroscopy for over 40 years.[5] High purity Ge (HPGe) detectors have evolved with resolution better than 0.4%.[6,7] However, to achieve such high performance, the small bandgap of HPGe detectors (0.7 eV) requires to be cooled to below 120 K in order to suppress the overwhelming leakage current associated with the thermal excitation of intrinsic charge carriers. In contrast, compound semiconductors, with the advantages of a broad range of stopping power and adjustable wide bandgaps, have been developed as more attractive options for room temperature detection. Mercuric iodide (HgI_2), cadmium telluride (CdTe), cadmium zinc telluride (CdZnTe), Gallium Arsenide (GaAs), Lead Iodide (PbI_2)[8–11] are common compound semiconductors for gamma-ray detection. Due to its good electron transport properties (10^{-3}–10^{-2} $cm^2\ V^{-1}$ mobility-lifetime product[12]), a high band gap (1.5–1.6 eV) and high resistivity ($\geq 10^{10}$ Ω cm), CdZnTe has been the primary focus for research and commercialization as room temperature detectors. However, it is difficult to achieve low-cost, high-quality CdZnTe single crystals for large volume detectors due to the high concentration of dislocation walls (sub-grain boundaries), the presence of Te inclusions, Zinc segregation.[13–19] In addition to the material imperfections of CdZnTe single crystals, the melt processing growth method and post-growth thermal annealing inflate the production cost of the crystals.[20]

Recently, Lead halide perovskite materials have attracted substantial attention, not only because of the application in photovoltaics, light emitting diodes (LEDs), and photodetectors, but also because of the deployment in radiation detection. Perovskite materials possess impressive optical and electrical properties, including long charge-carrier diffusion lengths, tunable bandgaps (1.43–2.3 eV), low defect density, and high defect tolerance.[21–24] Due to the presence of Pb, Br or I atoms, perovskite detector possesses large atomic number (Z) for strong stopping power, making them attractive for radiation detection. Additionally, the cheap raw materials coupled with low-cost solution growth methods to still achieve a large electron and hole mobility-lifetime ($\mu\tau$) product make perovskite materials highly competitive with CdZnTe.[25] Few significant works using

[a] Department of Applied Physical Sciences, The University of North Carolina at Chapel Hill, Chapel Hill, North Carolina, 27514, USA. E-mail: jhuang@unc.edu
[b] Nuclear Engineering Program, Department of Mechanical and Aerospace Engineering, The Ohio State University, Columbus, Ohio, 43210, USA

† Electronic supplementary information (ESI) available. See DOI: 10.1039/d0tc02706e

perovskites for gamma-ray detection have been reported over the past few years. Y. Sergii *et al.* fabricated the formamidinium lead triiodide ($FAPbI_3$) single crystal detector capable of sensing 59.6 keV ^{241}Am signal.[26] However, unintentional doping in perovskite materials makes the measured resistivities smaller than those calculated from intrinsic charge concentration.[27] The resistivity of hybrid perovskite can be further increased by improving the crystal quality or exploring other compositions. For example, H. Wei *et al.* utilized the weak p-doping property of $MAPbBr_3$, and partially replace Br- with Cl- to n-dope $MAPbBr_3$ and reduce the intrinsic carrier concentration.[28] The dopant-compensated $MAPbBr_{2.94}Cl_{0.06}$ alloy has over ten-fold improved bulk resistivity of 3.6×10^9 Ω cm, compared to 2×10^8 Ω cm of pristine $MAPbBr_3$. Alloying also improves the hole mobility to 560 $cm^2\ V^{-1}\ s^{-1}$, resulting in a higher $\mu\tau$ product of 1.8×10^{-2} $cm^2\ V^{-1}$. With the deposition of a guard ring, the detector can obtain ^{137}Cs energy spectrum with a resolution of 6.5%. This work also proved that single-crystalline hybrid perovskites have good stability against heat and moisture. But all-inorganic perovskite in principle may have better moisture/temperature stability, because of the alternation of organic cations by Cs cations.[29,30] Remarkable progress has been achieved by using Bridgman method to grow large-size and high-quality $CsPbBr_3$ single crystals.[31–34] For example, C. Constantinos *et al.* used equimolar amounts of $PbBr_2$ and CsBr to synthesize orthorhombic $CsPbBr_3$ single crystals in the sealed fused silica ampule at 600 °C.[31] In 2018, Y. Hui *et al.* applied modified Bridgman method to synthesize $CsPbBr_3$ single crystal with hole and electron $\mu\tau$ product of 1.34×10^{-3} $cm^2\ V^{-1}$ and 8.77×10^{-4} $cm^2\ V^{-1}$, respectively.[35] The $CsPbBr_3$ detectors can achieve an energy resolution of 3.9% for 122 keV 57-Co gamma-ray and 3.8% for 662 keV ^{137}Cs gamma-ray at room temperature. However, the Bridgman melt-growth method needs to raise the temperature to over 500 °C and go through multiple purification processes to purify the raw material which significantly increase the fabrication cost to a level that is not necessarily lower than that of CdZnTe. This complex high-cost method drives the research of simple and inexpensive low-temperature solution growth methods which could also synthesis high-quality crystals for the application of gamma-ray detection. There are few works demonstrating solution-grown $CsPbBr_3$ single crystals.[36,37] R. Yevgeny *et al.* and Z. Hongjian *et al.* employed antisolvent vapor assisted (ASV) method by using acetonitrile (MeCN) or methanol (MeOH).[38,39] N. Dmitry *et al.*, W. Fangbao *et al.*, and Z. Hongjian *et al.* used DMSO/DMF/cyclohexanol (CyOH) mixed solvent to widen the temperature range of solubility drop, and employed inverse temperature crystallization (ITC) method to grow large $CsPbBr_3$ single crystals.[40–42]

Here we report a simple additive assisted inverse temperature crystallization method to achieve high quality $CsPbBr_3$ single crystals. The addition of choline bromide (CB) into the precursor solution enables the growth of large, cuboid shape $CsPbBr_3$ crystals while using low purity raw materials. In comparison with crystals grown without CB, the density of traps in the crystals using this modified method are suppressed by an order of magnitude. The detectors made utilizing the solution-grown perovskite $CsPbBr_3$ single crystals acquired an energy spectrum from a cesium-137 (^{137}Cs) source with a resolution of 5.5% at 662 keV.

Results and discussion

Pioneering studies have reported that lead halide perovskite, such as $MAPbX_3$ (X = Br^- and I^-), $FAPbX_3$, and $CsPbBr_3$, show retrograde solubility in solvents like gamma-butyrolactone (GBL), *N*,*N*-dimethylformamide (DMF) and dimethyl sulfoxide (DMSO).[40,43–45] Therefore, we adopt the inverse temperature crystallization (ITC) method which crystalizes the $CsPbBr_3$ through elevating the temperature of the solution. For growth without additive, standard precursor solution was made by dissolving CsBr and $PbBr_2$ into DMSO solvent, as DMSO solvent has higher solubility limits for CsBr and $PbBr_2$ compared with GBL and DMF. For growth with CB additive, CB was further added into standard precursor solution. $CsPbBr_3$ single crystals were synthesized by gradually increasing the heating temperature. The molar ratio between $PbBr_2$ and CsBr is ~2 : 1 to obtain the pure $CsPbBr_3$ phase. It is reported that three possible products can be synthesized by tuning the $PbBr_2$: CsBr ratio.[37,40,46] If $PbBr_2$: CsBr is less than 1.5 : 1, Cs-rich precipitate (Cs_4PbBr_6) will be the main product. If $PbBr_2$: CsBr is larger than 4 : 1, a Pb-rich precipitate ($CsPb_2Br_5$) tends to be the primary product. This can be explained by that CsBr has lower solubility in DMSO than $PbBr_2$, while the formation of $PbBr_n^{(2-n)}$ by adding more $PbBr_2$ increases the solubility of CsBr.

$CsPbBr_3$ undergoes phase transitions from cubic to tetragonal at 130 °C, and from tetragonal to orthorhombic at 88 °C.[47,48] Fig. 1(a) displays its crystal structures at different temperature range. It possesses cubic structure (space group $Pm\bar{3}m$) at temperature higher than 130 °C. Upon cooling down below the first transition point, the $PbBr_6$ octahedra will rotate in the ab plane, forming tetragonal structure (space group *P*4/*mbm*). As the crystal is cooled past 88 °C, the structure transforms to an orthorhombic structure (space group *Pbnm*, a = 8.20 Å, b = 8.26 Å, c = 11.78 Å), involving $PbBr_6$ octahedra tilt away from c axis. Therefore, careful design of the growing temperature is required to avoid the defects and stress induced by phase transition.[49] In this work, we chose 85 °C as the growth temperature to ensure crystals keep growing at orthorhombic phase and thus there is no phase transformation once they are cooled down to room temperature.

Although we can control the crystal phase through growth temperature, the crystals grown from regular precursor solution (containing CsBr, $PbBr_2$, and DMSO) still suffer from bar shape, which is in accordance with previous reports.[39,50,51] Fig. 1(b) presents the photo of a bar shape $CsPbBr_3$ single crystal. The small bar shape makes it difficult to fabricate a practical detector. The bar shape mainly results from the asymmetric growth rate along different directions. To identify the various growth directions, we performed X-ray diffraction (XRD) and found the exposed facets to be (110), (1$\bar{1}$0), and (002), as shown

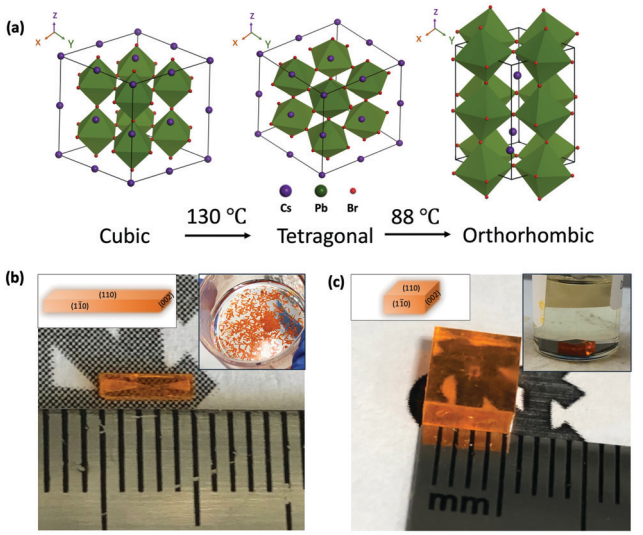

Fig. 1 (a) $CsPbBr_3$ structure at different temperature. The transition from cubic to tetragonal happens at 130 °C, and transition from tetragonal to orthorhombic happens at 88 °C. (b) Bar shape $CsPbBr_3$ single crystal grown without CB. The left inset indicates the miller indices of each surface, and the right inset is the photograph of crystals in solution. (c) Cuboid shape $CsPbBr_3$ single crystal grown with CB. The left inset indicates the miller indices of each surface, the right inset is the photograph of crystals in solution, and the bottom of the vial is a Si-wafer to make a flat bottom.

in the left inset of Fig. 1(b and c). The crystal is elongated along [002] direction, which can be attributed to the fastest growth rate along this direction.

To investigate the reason that $CsPbBr_3$ tends to grow faster along [002], we employed an attachment energy (AE) model developed by Hartman and Bennema, which has been widely used to predict crystal shape.[52–54] The attachment energy of a facet (*hkl*) is defined as the released energy when a new layer of atoms is attached to the surface of the crystal. The energy is determined by the bonding strength and the number of bonds at a given face. Therefore, faces with a larger attachment energy have faster growth rates. Here, in $CsPbBr_3$ orthorhombic structure, we mainly analyze $(1\bar{1}0)$ and (002) direction since the similarity in structure and growth rate of (110) and $(1\bar{1}0)$. Fig. 2(a) and (b) display the facets along [002] and $[1\bar{1}0]$, respectively. Two types of planes are presented normal to both directions. In particular, $PbBr_2$ terminated (002) facet with Pb : Br ratio of 2 : 1 and CsBr terminated (004) facet with Cs : Br ratio of 1 : 1 are presented normal to [002] direction. CsBr terminated $(1\bar{1}0)$ facet with Cs : Br of 1 : 1, and $PbBr_2$ terminated $(2\bar{2}0)$ facet with Pb : Br of 2 : 1 are presented normal to $[1\bar{1}0]$ direction. Here we employed first principle calculations by using CASTEP program which has plane-wave pseudopotential method to calculate the AE of these four facets.[55] The average AE of facets normal to the [002] direction was calculated to be 0.115 eV, 0.145 eV on (002) and 0.078 eV on (004). The average AE of the facets normal to $[1\bar{1}0]$ direction was calculated to be 0.095 eV, 0.084 eV on $(1\bar{1}0)$ and 0.110 eV on $(2\bar{2}0)$. The greater average AE calculated for facets along the [002] direction is congruent with the faster growth observed in the [002] direction of bar shaped crystals grown with no additives.

It is more favorable to have cuboid shape crystal to allow for easier fabrication and characterization of a detector. In this work, we found out that the addition of CB into precursor solution, containing CsBr, $PbBr_2$, CB and DMSO, could alter the resulting shape of the $CsPbBr_3$ crystals from a bar shape to a cuboid shape. As shown in Fig. 1(c), the cuboid crystal could maintain good transparency. The exposed facets were again characterized by XRD (Fig. 2(c)), and they all keep the same as the bar-shape crystal (left inset of Fig. 1(c)). Therefore, CB suppresses the [002] crystal growth rate without changing the $CsPbBr_3$ structure. Here we propose a possible mechanism by which CB is capable of altering the anisotropic growth typically observed for $CsPbBr_3$ single crystals. As shown in Fig. 2(d), CB is composed of quaternary ammonium group, a bromide ion, and a hydroxyl group. The positively charged quaternary ammonium group can coordinate with Br ions by electrostatic interactions, adsorb on the growing crystal, and subsequently block Cs^+ or Pb^{2+} attaching on the crystal growth site, illustrated in Fig. 2(e). Therefore, the crystal growth rate was reduced from 1.25 $mm^3\ h^{-1}$ in the solution without CB to 0.34 $mm^3\ h^{-1}$ in the solution with CB. It should be noted that it is possible for choline molecules to coordinate with not only the (002) surface but also the (110)/$(1\bar{1}0)$ surfaces, due to the equal plane density of Br ions. However, the change from cuboid shape to bar shape suggests growth of the [002] is more inhibited than [110]/$[1\bar{1}0]$. Because of the attachment of CB on those facets, the absorbing energy difference between these facets disappears. Therefore, crystals lose the preferred crystal growth direction. Here we demonstrate the addition of CB additives can be utilized to alter crystal growth to control the resulting crystal shape and produce attractive cuboid $CsPbBr_3$ solution processed single crystals.

We further investigated if additive-assisted method could improve the crystal quality. To understand how CB influences the defect density within the crystals, the trap density of states (tDOS) of $CsPbBr_3$ single crystal grown with and without CB was measured by thermal admittance spectroscopy, and the result is shown in Fig. 3(a). The CB-assisted growth process proves capable of drastically reducing the defect density of resulting crystals by roughly two orders of magnitude at low level traps states and approximately one order of magnitude at deeper trap states. In order to best characterize the quality of the crystal bulk, both types of crystals without obvious macroscopic defects were chosen in this measurement. Also, the surface of crystals was polished by sandpaper and passivated by $(C_8H_{17}NH_3)_2SO_4$ to eliminate any influence arising from differences at the surface.[56] This confirms that the CB-assisted ITC process is highly advantageous for not only altering the shape of the crystals, but also growing high-quality single crystals with reduced defect density.

It should be also noted that the concentration could impact the crystal defect density. Because the CB suppresses growth rate and decrease defect density by adsorbing on the surface of growing crystal. Small amount of CB could not offer enough quaternary ammonium groups if the size of the crystal is large. Therefore, we found obvious macroscopic defects at the edge of crystal due to the insufficient CB. In this work, the

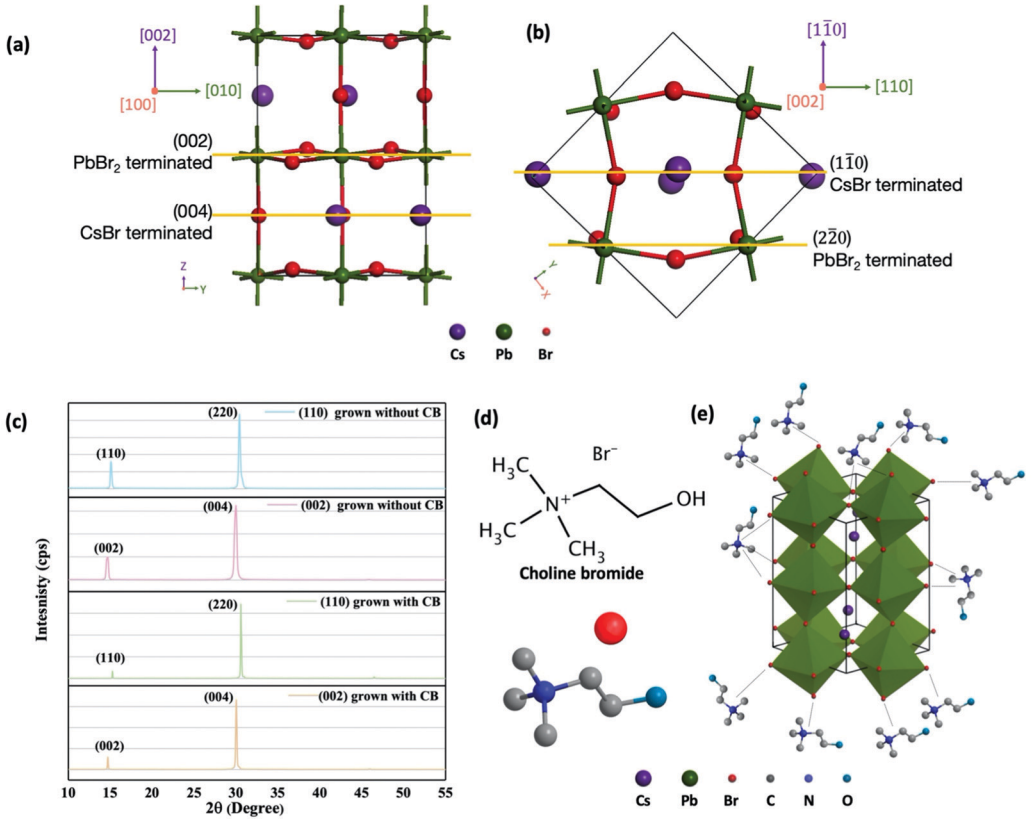

Fig. 2 (a) Side view of the orthorhombic $CsPbBr_3$ unit cell structure. The yellow lines indicate (002) and (004) plane. (b) Top view of the unit cell structure. The yellow lines indicate (1$\bar{1}$0) and (2$\bar{2}$0) plane. (c) XRD pattern of $CsPbBr_3$ single crystal grown with and without CB. (d) Molecular structure of choline bromide (CB). (e) Schematic illustration of CB assisted $CsPbBr_3$ single crystal growth.

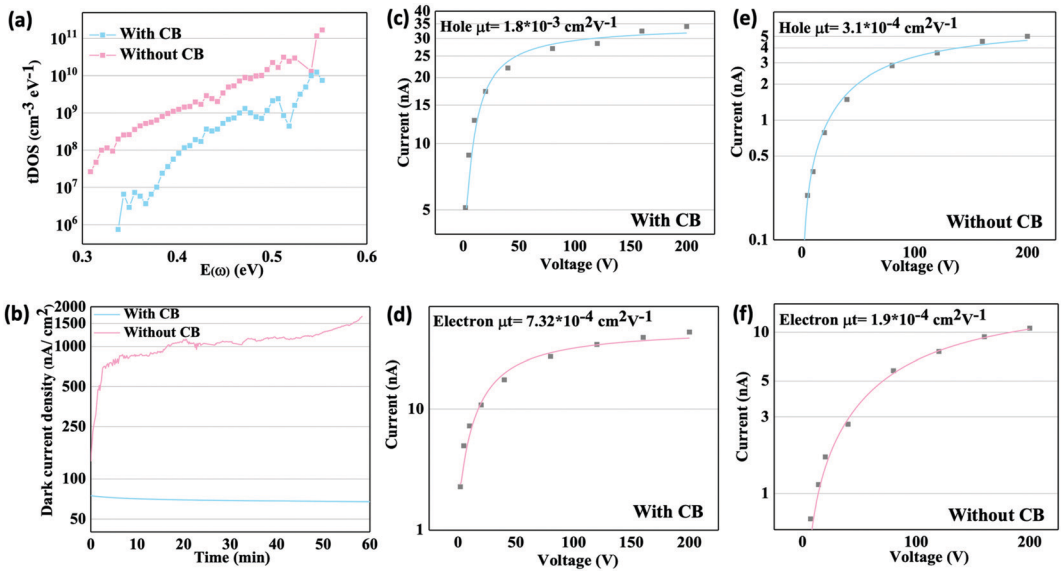

Fig. 3 (a) tDOS and (b) dark current density as function of time of detectors with and without CB. (c) hole and (d) electron μτ product of detector with CB by Hecht equation fitting. (e) hole and (f) electron μτ product of detector without CB by Hecht equation fitting.

concentration of CB was 0.09 mol L^{-1} CB, and typical size of crystal at this concentration is around 9 mm × 9 mm × 3 mm.

The improved quality of crystals grown using the CB-assisted ITC process is also evident in the resulting performance of the fabricated detectors. Detectors are fabricated by depositing electrodes, gold (Au) cathode and gallium (Ga) anode, at the center of the crystals to suppress the leakage current flowing at the side surface which could otherwise corrupt the signal, Fig. 4(a). It is

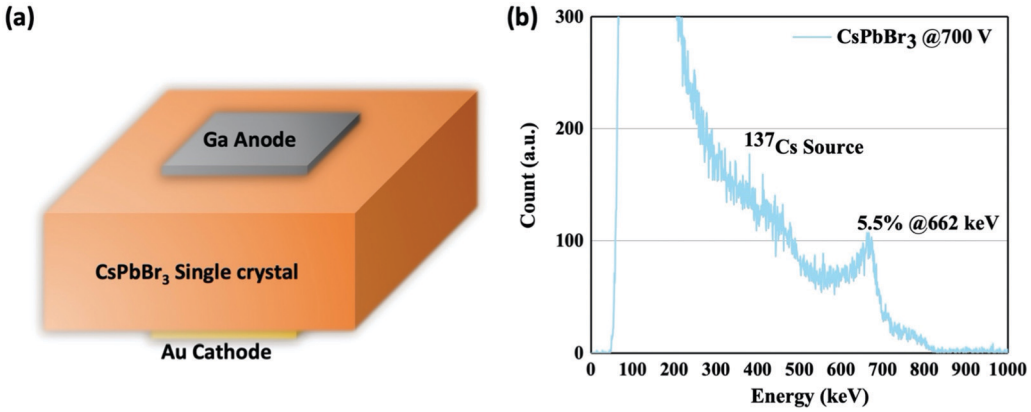

Fig. 4 (a) Schematic of detector structure (4.5 mm × 4.5 mm electrode area, 2.5 mm thickness). (b) 662 keV ^{137}Cs spectrum acquired by $CsPbBr_3$ single crystal under 700 V.

important to note that due to $CsPbBr_3$ being an intrinsically p-type material, Ga is chosen as the anode in order to decrease the dark current density under high electrical field by forming a Schottky contact at the Ga side under reverse bias.[21]

It is well reported that when under an electric field, ions within perovskite materials can migrate and result in a myriad of problems for all kinds of devices that need to be biased.[57,58] The presence of point defects, lattice distortion, and dislocations within the bulk of single crystals can facilitate ion migration.[59] Significant ion migration results in unstable dark current, known as dark current drift. Dark current drift can be particularly problematic for perovskite materials used in gamma-ray detection due to the extremely high applied voltage bias accelerating the ion migration process. Therefore, we can indirectly evaluate the crystal quality by assessing the dark current drift of the detectors. Detectors were biased under a large electric field of 910 V cm^{-1} and the dark current was recorded for one hour, as shown in Fig. 3(b). The dark current drift of detectors is effectively suppressed when using crystals grown using the CB-assisted method, resulting in a drift of only 6 nA cm^{-2} over one hour with a starting dark current of 74 nA cm^{-2}. In contrast, the dark current density of the resulting detector without using the CB-assisted method started at 135 nA cm^{-2} and drifted to 1703 nA cm^{-2}. The large dark current drift of the detector without CB is in consistent with the greater defect density shown in Fig. 3(a).

The mobility-lifetime ($\mu\tau$) product is one of the important figures of merit for gamma-ray detectors. According to Hecht equation, the mobility-lifetime is an intrinsic parameter of a material that determines the charge collection efficiency.[60] In this work, we use a 20 keV X-ray source to measure photocurrent at various voltages. Due to the high atomic density of $CsPbBr_3$, the mean free path of 20 keV X-rays is only ~30 μm (Linear attenuation coefficient-Photon energy plot in ESI,† Fig. S4). This means that the carriers are mainly generated near the surface of the 2.5 mm thick crystal. The $\mu\tau$ product is obtained by fitting the photocurrent I to the modified Hecht equation:

$$I = \frac{I_0 \mu\tau V}{d}\left(1 - \exp\left(-\frac{d^2}{\mu\tau V}\right)\right) \quad (1)$$

where d is the thickness of the detector, I_0 is the saturated photocurrent, and V is the voltage bias applied to the detector. The hole and electron $\mu\tau$ products of the detector using a crystal grown from the CB-assisted method are then calculated to be 1.80 × 10^{-3} cm^2 V^{-1} (Fig. 3(c)) and 0.73 × 10^{-3} cm^2 V^{-1} (Fig. 3(d)), respectively. In contrast, the calculated hole and electron $\mu\tau$ products of the detector using a crystal grown from the standard ITC method are just 0.31 × 10^{-3} cm^2 V^{-1} (Fig. 3(e)) and 0.19 × 10^{-3} cm^2 V^{-1}, respectively (Fig. 3(f)). The use of crystals grown by the new CB-assisted ITC process improves the $\mu\tau$ products of the resulting detector by approximately 4 times. The mobility of the detector fabricated with the CB-assisted crystals was also measured by the time-of-flight technique (ToF). The electron and hole mobility estimated by linear fitting $\tau_{transit}$ *versus* $1/V$ are 181 cm^2 V^{-1} s^{-1} (ESI,† Fig. S5) and 56.5 cm^2 V^{-1} s^{-1} (ESI,† Fig. S6), respectively. These values are comparable to the mobility of $CsPbBr_3$ crystal by Bridgman growth approach.[35]

The high atomic density, low trap density, stable dark current, and large $\mu\tau$ product suggest that CB-assisted $CsPbBr_3$ single crystal detectors have immense potential for gamma-ray spectroscopy. To this end, we tested gamma-ray spectral performance under exposure to a ^{137}Cs source emitting 662 keV gamma-rays. For the measurement, the ^{137}Cs source was placed on the Au cathode side of $CsPbBr_3$ detector (4.5 mm × 4.5 mm electrode area, 2.5 mm thickness), which was connected to a Charge Sensitive Preamplifier (CAEN A1422) and a CAEN N6724 Digitizer with embedded Digital Pulse Processing firmware. The typical resolution acquired by the CB-assisted $CsPbBr_3$ detector is 9–10%, while the best resolution acquired at room temperature is 5.5% (Fig. 4(b)) with bias of 2700 V cm^{-1} and collection time of 15 min. It should be noted that low purity grade raw materials directly purchased from vendor were used to grow the single crystal, which could potentially be a source of undesirable impurities in the final crystal. It is expected that the performance and resolution of the detector can be further improved if high purity raw materials are used.[35] The elevated Compton plateau in Fig. 4(b) can be attributed to the small volume of the crystal, resulting in a large fraction of scattered photons likely escaping from the detector. Therefore, future

work can be focused scaling the additive assisted ITC solution growth process to produce larger crystals.

In conclusion, we demonstrate that high quality $CsPbBr_3$ single crystals can be synthesized by using our new additive-assisted ITC solution growth method. The addition of choline bromide into the precursor solution is able to mediate the crystallization process to suppress the fast growth along [002] direction, thus reforming the shape of the resulting crystal from bar to cuboid. CB-assisted grown $CsPbBr_3$ single crystals also exhibit lower trap density, and superior dark current stability, indicative of a higher quality crystal compared to those grown without CB. The CB-assisted $CsPbBr_3$ single crystal detector also demonstrates excellent charge transport capabilities. Estimated by Hecht equation, the electron and hole mobility-lifetime ($\mu\tau$) products are 0.73×10^{-3} cm^2 V^{-1} and 1.80×10^{-3} cm^2 V^{-1}, respectively. More importantly, the CB-assisted $CsPbBr_3$ single crystal is able to deliver a 662 keV ^{137}Cs spectrum with resolution of 5.5%, which is, to date, the highest resolution acquired by a solution grown perovskite detector.

Experimental section

Chemicals and reagents

Low purity $PbBr_2$ ($\geq$98%), CsBr ($\geq$99.9%), dimethyl sulfoxide (DMSO, $\geq$99.9%) were purchased from Sigma-Aldrich. Choline Bromide (CB, $\geq$98%) was purchased from TCI America. All raw materials and solvent were not further purified before using.

Preparation of precursor solution

Standard $CsPbBr_3$ precursor solution was obtained by dissolving CsBr (4.8 mmol) and $PbBr_2$ (9.6 mmol) with a molar ratio of 1 : 2 in 5.3 mL DMSO solution. Precursor solution with CB was obtained by further adding 0.5 mmol CB to the standard precursor solution. The precursor solutions were heated to 80 °C to accelerate the dissolution of the raw material. Transparent solutions could be obtained after 5–10 hours. Solutions were then filtered with a 0.2 μm pore size PTFE filter.

Growth of $CsPbBr_3$ single crystal

Small $CsPbBr_3$ seeds were first prepared with fresh supersaturated precursor solution at 85 °C. Small and transparent seeds were then picked and put on the bottom of the vials for large crystal growth. The temperature of the vials was set at 80 °C initially with an increasing rate of 1 °C h^{-1}, and was eventually maintained at 85 °C. Vials were covered with glass slides to avoid fast evaporation of the DMSO. So the growth driving force is supersaturation achieved by slow evaporation of DMSO solvent. After 120–170 hours, a centimeter-sized single crystal was picked from the solution, followed by wiping the residue solution on the surface.

Detector fabrication

The resulting orange $CsPbBr_3$ crystals were fine polished with 14 000 grit polishing paper by the polishing machine. The dust on the polished surface was removed by nitrogen flow and washed by Toluene. The surface of the crystals was then spin-coated by $(C_8H_{17}NH_3)_2SO_4$ for 2500 rpm to convert perovskite into lead sulfate ($PbSO_4$) passivation layer, which is insoluble in water and large band gap. More details of the passivation can be found in our previous work.[56] One side of the crystals was deposited with gold (Au) with a thickness of 50 nm by thermal evaporation. The other side was applied with gallium (Ga).

Characterization

The X-ray diffraction (XRD) was characterized by Rigaku Mini-Flex X-ray diffractometer. Steady-state PL measurement was performed on a Horiba iHR320 imaging spectrometer at 25 °C. The excitation source was a 325 nm pulse laser. Dark current was measured by a Keithley 2400 Source meter with a sampling rate of 500 ms per point. Trap density of states (tDOS) was measured by admittance spectroscopy method, the device was kept dark during the entire test. The test was performed by an Agilent E4980A Precision LCR Meter. The energy profile of tDOS was calculated from the equation $N_T(E_\omega) = -\frac{1}{qk_BT}\frac{\omega dC}{d\omega}\frac{V_{bi}}{W}$, where q is the elementary charge, ω is the angular frequency of the ac bias, C is the specific capacitance of the device, T is the temperature, k_B is the Boltzmann constant, W is depletion width of the device, V_{bi} is the built-in potential. The energetic demarcation is derived by $E_\omega = k_BT\ln\frac{\omega_0}{\omega}$, where ω_0 is the attempt-to-escape frequency. Mobility is obtained by the time-of-flight (ToF) technique. The excitation source was a 325 nm pulse laser. The photocurrent induced by laser was first fed into a SR-570 current pre-amplifie, and then recorded with an Agilent DSO-X 3104A digital oscilloscope. Mobility-lifetime ($\mu\tau$) product was fitted from modified Hecht equation $I = \frac{I_0\mu\tau V}{d}\left(1 - \exp\left(-\frac{d^2}{\mu\tau V}\right)\right)$. The photocurrent is generated by a 20 keV X-ray beam. Sensitivity was measured under a different dose rate of 60 keV X-ray source. The radiation dose rate was calibrated by a RaySafe X2 dosimeter. Gamma-ray spectrum is collected by a Charge Sensitive Preamplifier (CAEN A1422), a CAEN N6724 Digitizer, and its embedded Digital Pulse Processing firmware.[61]

Conflicts of interest

There are no conflicts to declare.

Acknowledgements

This research project is sponsored by the Department of the Defense, Defense Threat Reduction Agency under Grant HDTRA1170054. The content of the information does not necessarily reflect the position or the policy of the federal government, and no official endorsement should be inferred.

References

1 J. Hugg, B. Harris and H. Tomita, Evaluation of CZT gamma cameras for human SPECT and small FOV imaging, *J. Nucl. Med.*, 2018, **59**(suppl. 1), 220.

2 N. Gehrels, G. Chincarini, P. Giommi, K. O. Mason, J. A. Nousek, A. A. Wells, N. E. White, S. D. Barthelmy, D. N. Burrows, L. R. Cominsky, K. C. Hurley, F. E. Marshall, P. Meszaros, P. W. A. Roming, L. Angelini, L. M. Barbier, T. Belloni, S. Campana, P. A. Caraveo, M. M. Chester, O. Citterio, T. L. Cline, M. S. Cropper, J. R. Cummings, A. J. Dean, E. D. Feigelson, E. E. Fenimore, D. A. Frail, A. S. Fruchter, G. P. Garmire, K. Gendreau, G. Ghisellini, J. Greiner, J. E. Hill, S. D. Hunsberger, H. A. Krimm, S. R. Kulkarni, P. Kumar, F. Lebrun, N. M. Lloyd-Ronning, C. B. Markwardt, B. J. Mattson, R. F. Mushotzky, J. P. Norris, J. Osborne, B. Paczynski, D. M. Palmer, H. S. Park, A. M. Parsons, J. Paul, M. J. Rees, C. S. Reynolds, J. E. Rhoads, T. P. Sasseen, B. E. Schaefer, A. T. Short, A. P. Smale, I. A. Smith, L. Stella, G. Tagliaferri, T. Takahashi, M. Tashiro, L. K. Townsley, J. Tueller, M. J. L. Turner, M. Vietri, W. Voges, M. J. Ward, R. Willingale, F. M. Zerbi and W. W. Zhang, The Swift gamma-ray burst mission, *Astrophys. J.*, 2004, **611**(2), 1005–1020.

3 K. Iniewski, CZT detector technology for medical imaging, *J. Instrum.*, 2014, **9**, C11001.

4 M. S. Pravikoff, C. Marquet and P. Hubert, Dating of wines with cesium-137: Fukushima's imprint, 2018, arXiv preprint arXiv:1807.04340.

5 A. Tavendale, Large germanium lithium-drift pin diodes for gamma-ray spectroscopy, *IEEE Trans. Nucl. Sci.*, 1965, **12**(1), 255–264.

6 P. Sangsingkeow, K. D. Berry, E. J. Dumas, T. W. Raudorf and T. A. Underwood, Advances in germanium detector technology, *Nucl. Instrum. Methods Phys. Res., Sect. A*, 2003, **505**(1–2), 183–186.

7 R. Cooper, M. Amman and K. Vetter, High resolution gamma-ray spectroscopy at high count rates with a prototype high purity germanium detector, *Nucl. Instrum. Methods Phys. Res., Sect. A*, 2018, **886**, 1–6.

8 J. F. Butler, S. J. Friesenhahn, C. L. Lingren, B. A. Apotovsky, F. P. Doty, W. L. Ashburn and W. P. Dillon, In $Cd_{1-x}Zn_x$ Te detector imaging array, Medical Imaging 1993: Physics of Medical Imaging, *International Society for Optics and Photonics*, 1993, pp. 30–38.

9 J. S. Iwanczyk, W. F. Schnepple and M. J. Masterson, The Effect of Charge Trapping on the Spectrometric Performance of Hgi2 Gamma-Ray Detectors, *Nucl. Instrum. Methods Phys. Res., Sect. A*, 1992, **322**(3), 421–426.

10 V. Deich and M. Roth, Improved performance lead iodide nuclear radiation detectors, *Nucl. Instrum. Methods Phys. Res., Sect. A*, 1996, **380**(1-2), 169–172.

11 H. Malm, T. Raudorf, M. Martini and K. Zanio, Gamma ray efficiency comparisons for Si (Li), Ge, CdTe and HgI2 detectors, *IEEE Trans. Nucl. Sci.*, 1973, **20**(1), 500–509.

12 L. Li, F. Lu, K. Shah, M. Squillante, L. Cirignano, W. Yao, R. W. Olson, P. Luke, Y. Nemirovsky, A. Burger, G. Wright and R. B. James, A new method for growing detector-grade cadmium zinc telluride crystals, *2001 Ieee Nuclear Science Symposium, Conference Records*, 2002, vol. 1–4, pp. 2396–2400.

13 U. N. Roy, G. S. Camarda, Y. Cui, R. Gul, A. Hossain, G. Yang, J. Zazvorka, V. Dedic, J. Franc and R. B. James, Role of selenium addition to CdZnTe matrix for room-temperature radiation detector applications, *Sci. Rep.*, 2019, **9**, 1620.

14 A. E. Bolotnikov, G. S. Camarda, G. A. Carini, Y. Cui, K. T. Kohman, L. Li, M. B. Salomon and R. B. James, Performance-limiting defects in CdZnTe detectors, *IEEE Trans. Nucl. Sci.*, 2007, **54**(4), 821–827.

15 A. E. Bolotnikov, S. Babalola, G. S. Camarda, Y. G. Cui, S. U. Egarievwe, R. Hawrami, A. Hossain, G. Yang and R. B. James, Te Inclusions in CZT Detectors: New Method for Correcting Their Adverse Effects, *IEEE Trans. Nucl. Sci.*, 2010, **57**(2), 910–919.

16 J. K. Radhakrishnan, B. S. Sunderseshu, M. Srivastava, G. L. Seth, R. Raman, R. C. Narula and R. K. Bagai, Homogenization of zinc distribution in vertical Bridgman grown Cd(0.96)Zn(0.04)Te crystals, *Bull. Mater. Sci.*, 2001, **24**(6), 659–663.

17 N. Zhang, A. Yeckel, A. Burger, Y. L. Cui, K. G. Lynn and J. J. Derby, Anomalous segregation during electrodynamic gradient freeze growth of cadmium zinc telluride, *J. Cryst. Growth*, 2011, **325**(1), 10–19.

18 A. Hossain, A. E. Bolotnikov, G. S. Camarda, Y. Cui, G. Yang and R. B. James, Defects in cadmium zinc telluride crystals revealed by etch-pit distributions, *J. Cryst. Growth*, 2008, **310**(21), 4493–4498.

19 U. N. Roy, S. Weiler, J. Stein, Y. Cui, M. Groza, V. Buliga and A. Burger, Zinc mapping in THM grown detector grade CZT, *J. Cryst. Growth*, 2012, **347**(1), 53–55.

20 S. U. Egarievwe, G. Yang, A. A. Egarievwe, I. O. Okwechime, J. Gray, Z. M. Hales, A. Hossain, G. S. Camarda, A. E. Bolotnikov and R. B. James, Post-growth annealing of Bridgman-grown CdZnTe and CdMnTe crystals for room-temperature nuclear radiation detectors, *Nucl. Instrum. Methods Phys. Res., Sect. A*, 2015, **784**, 51–55.

21 Q. F. Dong, Y. J. Fang, Y. C. Shao, P. Mulligan, J. Qiu, L. Cao and J. S. Huang, Electron-hole diffusion lengths >175 μm in solution-grown $CH_3NH_3PbI_3$ single crystals, *Science*, 2015, **347**(6225), 967–970.

22 G. E. Eperon, S. D. Stranks, C. Menelaou, M. B. Johnston, L. M. Herz and H. J. Snaith, Formamidinium lead trihalide: a broadly tunable perovskite for efficient planar heterojunction solar cells, *Energy Environ. Sci.*, 2014, **7**(3), 982–988.

23 D. Shi, V. Adinolfi, R. Comin, M. J. Yuan, E. Alarousu, A. Buin, Y. Chen, S. Hoogland, A. Rothenberger, K. Katsiev, Y. Losovyj, X. Zhang, P. A. Dowben, O. F. Mohammed, E. H. Sargent and O. M. Bakr, Low trap-state density and long carrier diffusion in organolead trihalide perovskite single crystals, *Science*, 2015, **347**(6221), 519–522.

24 J. Kang and L. W. Wang, High Defect Tolerance in Lead Halide Perovskite CsPbBr3, *J. Phys. Chem. Lett.*, 2017, **8**(2), 489–493.

25 H. T. Wei and J. S. Huang, Halide lead perovskites for ionizing radiation detection, *Nat. Commun.*, 2019, **10**, 1066.

26 S. Yakunin, D. N. Dirin, Y. Shynkarenko, V. Morad, I. Cherniukh, O. Nazarenko, D. Kreil, T. Nauser and M. V. Kovalenko, Detection of gamma photons using

solution-grown single crystals of hybrid lead halide perovskites, *Nat. Photonics*, 2016, **10**(9), 585–589.

27 Q. Wang, Y. C. Shao, H. P. Xie, L. Lyu, X. L. Liu, Y. L. Gao and J. S. Huang, Qualifying composition dependent p and n self-doping in CH3NH3PbI3, *Appl. Phys. Lett.*, 2014, **105**(16), 163508.

28 H. T. Wei, D. DeSantis, W. Wei, Y. H. Deng, D. Y. Guo, T. J. Savenije, L. Cao and J. S. Huang, Dopant compensation in alloyed $CH_3NH_3PbBr_{3-x}Cl_x$ perovskite single crystals for gamma-ray spectroscopy, *Nat. Mater.*, 2017, **16**(8), 826–833.

29 K. A. Bush, C. D. Bailie, Y. Chen, A. R. Bowring, W. Wang, W. Ma, T. Leijtens, F. Moghadam and M. D. McGehee, Thermal and Environmental Stability of Semi-Transparent Perovskite Solar Cells for Tandems Enabled by a Solution-Processed Nanoparticle Buffer Layer and Sputtered ITO Electrode, *Adv. Mater.*, 2016, **28**(20), 3937–3943.

30 S. N. Habisreutinger, T. Leijtens, G. E. Eperon, S. D. Stranks, R. J. Nicholas and H. J. Snaith, Carbon Nanotube/Polymer Composites as a Highly Stable Hole Collection Layer in Perovskite Solar Cells, *Nano Lett.*, 2014, **14**(10), 5561–5568.

31 C. C. Stoumpos, C. D. Malliakas, J. A. Peters, Z. F. Liu, M. Sebastian, J. Im, T. C. Chasapis, A. C. Wibowo, D. Y. Chung, A. J. Freeman, B. W. Wessels and M. G. Kanatzidis, Crystal Growth of the Perovskite Semiconductor CsPbBr3: A New Material for High-Energy Radiation Detection, *Cryst. Growth Des.*, 2013, **13**(7), 2722–2727.

32 P. Zhang, Q. H. Sun, Y. D. Xu, X. Li, L. Liu, G. D. Zhang and X. T. Tao, Enhancing Carrier Transport Properties of Melt-grown CsPbBr3 Single Crystals by Eliminating Inclusions, *Cryst. Growth Des.*, 2020, **20**(4), 2424–2431.

33 M. Z. Zhang, Z. P. Zheng, Q. Y. Fu, Z. Chen, J. L. He, S. Zhang, L. Yan, Y. X. Hu and W. Luo, Growth and characterization of all-inorganic lead halide perovskite semiconductor CsPbBr3 single crystals, *CrystEngComm*, 2017, **19**(45), 6797–6803.

34 J. Z. Song, Q. Z. Cui, J. H. Li, J. Y. Xu, Y. Wang, L. M. Xu, J. Xue, Y. H. Dong, T. Tian, H. D. Sun and H. B. Zeng, Ultralarge All-Inorganic Perovskite Bulk Single Crystal for High-Performance Visible-Infrared Dual-Modal Photodetectors, *Adv. Opt. Mater.*, 2017, **5**(12), 1700157.

35 Y. H. He, L. Matei, H. J. Jung, K. M. McCall, M. Chen, C. C. Stoumpos, Z. F. Liu, J. A. Peters, D. Y. Chung, B. W. Wessels, M. R. Wasielewski, V. P. Dravid, A. Burger and M. G. Kanatzidis, High spectral resolution of gamma-rays at room temperature by perovskite $CsPbBr_3$ single crystals, *Nat. Commun.*, 2018, **9**, 1609.

36 J. X. Ding, S. J. Du, Z. Y. Zuo, Y. Zhao, H. Z. Cui and X. Y. Zhan, High Detectivity and Rapid Response in Perovskite $CsPbBr_3$ Single-Crystal Photodetector, *J. Phys. Chem. C*, 2017, **121**(9), 4917–4923.

37 M. I. Saidaminov, M. A. Haque, J. Almutlaq, S. Sarmah, X. H. Miao, R. Begum, A. A. Zhumekenov, I. Dursun, N. Cho, B. Murali, O. F. Mohammed, T. Wu and O. M. Bakr, Inorganic Lead Halide Perovskite Single Crystals: Phase-Selective Low-Temperature Growth, Carrier Transport Properties, and Self-Powered Photodetection, *Adv. Opt. Mater.*, 2017, **5**, 2.

38 Y. Rakita, N. Kedem, S. Gupta, A. Sadhanala, V. Kalchenko, M. L. Bohm, M. Kulbak, R. H. Friend, D. Cahen and G. Hodes, Low-Temperature Solution-Grown CsPbBr3 Single Crystals and Their Characterization, *Cryst. Growth Des.*, 2016, **16**(10), 5717–5725.

39 H. J. Zhang, X. Liu, J. P. Dong, H. Yu, C. Zhou, B. B. Zhang, Y. D. Xu and W. Q. Jie, Centimeter-Sized Inorganic Lead Halide Perovskite $CsPbBr_3$ Crystals Grown by an Improved Solution Method, *Cryst. Growth Des.*, 2017, **17**(12), 6426–6431.

40 D. N. Dirin, I. Cherniukh, S. Yakunin, Y. Shynkarenko and M. V. Kovalenko, Solution-Grown CsPbBr3 Perovskite Single Crystals for Photon Detection, *Chem. Mater.*, 2016, **28**(23), 8470–8474.

41 F. B. Wang, H. J. Zhang, Q. H. Sun, A. Ben Hafsia, Z. X. Chen, B. B. Zhang, Y. D. Xu and W. Q. Jie, Low-Temperature Solution Growth and Characterization of Halogen (Cl, I)-Doped $CsPbBr_3$ Crystals, *Cryst. Growth Des.*, 2020, **20**(3), 1638–1645.

42 H. J. Zhang, F. B. Wang, Y. F. Lu, Q. H. Sun, Y. D. Xu, B. B. Zhang, W. Q. Jie and M. G. Kanatzidis, High-sensitivity X-ray detectors based on solution-grown caesium lead bromide single crystals, *J. Mater. Chem. C*, 2020, **8**(4), 1248–1256.

43 M. I. Saidaminov, A. L. Abdelhady, B. Murali, E. Alarousu, V. M. Burlakov, W. Peng, I. Dursun, L. F. Wang, Y. He, G. Maculan, A. Goriely, T. Wu, O. F. Mohammed and O. M. Bakr, High-quality bulk hybrid perovskite single crystals within minutes by inverse temperature crystallization, *Nat. Commun.*, 2015, **6**, 7586.

44 H. T. Wei, Y. J. Fang, P. Mulligan, W. Chuirazzi, H. H. Fang, C. C. Wang, B. R. Ecker, Y. L. Gao, M. A. Loi, L. Cao and J. S. Huang, Sensitive X-ray detectors made of methylammonium lead tribromide perovskite single crystals, *Nat. Photonics*, 2016, **10**(5), 333–339.

45 M. I. Saidaminov, A. L. Abdelhady, G. Maculan and O. M. Bakr, Retrograde solubility of formamidinium and methylammonium lead halide perovskites enabling rapid single crystal growth, *Chem. Commun.*, 2015, **51**(100), 17658–17661.

46 M. Liu, J. T. Zhao, Z. L. Luo, Z. H. Sun, N. Pan, H. Y. Ding and X. P. Wang, Unveiling Solvent-Related Effect on Phase Transformations in CsBr- PbBr2 System: Coordination and Ratio of Precursors, *Chem. Mater.*, 2018, **30**(17), 5846–5852.

47 S. Hirotsu, J. Harada, M. Iizumi and K. Gesi, Structural phase transitions in CsPbBr3, *J. Phys. Soc. Jpn.*, 1974, **37**(5), 1393–1398.

48 P. Cottingham and R. L. Brutchey, Depressed Phase Transitions and Thermally Persistent Local Distortions in CsPbBr3 Quantum Dots, *Chem. Mater.*, 2018, **30**(19), 6711–6716.

49 S. A. T. Redfern, High-temperature structural phase transitions in perovskite ($CaTiO_3$), *J. Phys.: Condens. Matter*, 1996, **8**(43), 8267–8275.

50 C. Y. Zhao, W. M. Tian, J. X. Li, Q. Sun, J. J. Luo, H. Yuan, B. D. Gai, J. Tang, J. W. Guo and S. Y. Jin, Stable Two-Photon Pumped Amplified Spontaneous Emission from Millimeter-Sized CsPbBr3 Single Crystals, *J. Phys. Chem. Lett.*, 2019, **10**(10), 2357–2362.

51 V. V. Belykh, D. R. Yakovlev, M. M. Glazov, P. S. Grigoryev, M. Hussain, J. Rautert, D. N. Dirin, M. V. Kovalenko and

M. Bayer, Coherent spin dynamics of electrons and holes in $CsPbBr_3$ perovskite crystals, *Nat. Commun.*, 2019, **10**, 673.
52 P. Hartman and P. Bennema, The attachment energy as a habit controlling factor: I. Theoretical considerations, *J. Cryst. Growth*, 1980, **49**(1), 145–156.
53 J. J. Li, C. J. Tilbury, S. H. Kim and M. F. Doherty, A design aid for crystal growth engineering, *Prog. Mater. Sci.*, 2016, **82**, 1–38.
54 D. S. Coombes, C. R. A. Catlow, J. D. Gale, A. L. Rohl and S. L. Price, Calculation of attachment energies and relative volume growth rates as an aid to polymorph prediction, *Cryst. Growth Des.*, 2005, **5**(3), 879–885.
55 S. J. Clark, M. D. Segall, C. J. Pickard, P. J. Hasnip, M. I. Probert, K. Refson and M. C. Payne, First principles methods using CASTEP, *Z. Kristallogr. – Cryst. Mater.*, 2005, **220**(5/6), 567–570.
56 S. Yang, S. S. Chen, E. Mosconi, Y. J. Fang, X. Xiao, C. C. Wang, Y. Zhou, Z. H. Yu, J. J. Zhao, Y. L. Gao, F. De Angelis and J. S. Huang, Stabilizing halide perovskite surfaces for solar cell operation with wide-bandgap lead oxysalts, *Science*, 2019, **365**(6452), 473–478.
57 B. Chen, P. N. Rudd, S. Yang, Y. B. Yuan and J. S. Huang, Imperfections and their passivation in halide perovskite solar cells, *Chem. Soc. Rev.*, 2019, **48**(14), 3842–3867.
58 Y. B. Yuan and J. S. Huang, Ion Migration in Organometal Trihalide Perovskite and Its Impact on Photovoltaic Efficiency and Stability, *Acc. Chem. Res.*, 2016, **49**(2), 286–293.
59 Y. Yuan and J. Huang, Ion migration in organometal trihalide perovskite and its impact on photovoltaic efficiency and stability, *Acc. Chem. Res.*, 2016, **49**(2), 286–293.
60 K. Hecht, Zum Mechanismus des lichtelektrischen Primärstromes in isolierenden Kristallen, *Z. Phys.*, 1932, **77**(3-4), 235–245.
61 L. Pan, Y. X. Feng, P. Kandlakunta, J. S. Huang and L. R. Cao, Performance of Perovskite CsPbBr3 Single Crystal Detector for Gamma-Ray Detection, *IEEE Trans. Nucl. Sci.*, 2020, **67**(2), 443–449.

